Projectile fragmentation of ^{129}Xe at $E_{\text{lab}}=790A$ MeV

J. Reinhold,* J. Friese, H.-J. Körner, R. Schneider, and K. Zeitelhack
Physikdepartment E12, Technische Universität München, D-85747 Garching, Germany

H. Geissel, A. Magel, G. Münzenberg, and K. Sümmerer
Gesellschaft für Schwerionenforschung, D-64220 Darmstadt, Germany
(Received 20 January 1998)

We have measured production yields and longitudinal momentum distributions of projectilelike fragments in the reaction ^{129}Xe + ^{27}Al at an energy of $E_{\text{lab}}=790A$ MeV. Production cross sections higher than expected from systematics were observed for nuclei in the neutron-deficient tails of the isotopic distributions. A comparison with previously measured data from the fragmentation of ^{136}Xe ions shows that the production yields strongly depend on the neutron excess of the projectile with respect to the line of β stability. The momentum distributions exhibit a dependence on the fragment neutron-to-proton ratio in isobaric chains, which was not expected from systematics so far. This can be interpreted by a higher excitation of the projectile during the formation of neutron-deficient fragments. [S0556-2813(98)02507-2]

PACS number(s): 25.70.Mn

I. INTRODUCTION

Numerous studies have shown that projectile fragmentation at high energies is a powerful tool to produce intensive beams of exotic nuclei even close to the driplines [1]. In order to get a quantitative estimate of the production cross sections of exotic nuclei, empirical parametrizations have been developed and fitted to the available experimental data (e.g., Refs. [2–4]). Important for the planning of future experiments is, whether these parametrizations yield reliable predictions even for very exotic nuclei in the tails of the isotopic distributions, where experimental data are sparse. Also of considerable interest for the study of nuclei at the borderline of stability is whether the isotopic yields may be influenced by the use of appropriate neutron-rich or neutron-deficient projectiles. Experiments which measured the fragmentation of different isobaric projectiles (or targets) showed a shift of the fragment distributions, which is related to the projectile (target) neutron or proton excess relative to the line of β stability [5–7]. This "memory effect" has been included quantitatively in the EPAX parametrization [3], but only few data from light projectiles were available to fit the corresponding parameters. Nevertheless this parametrization described successfully the fragmentation yields from the neutron rich isotope ^{86}Kr [8]. More recently, Pfaff *et al.* came to very similar conclusions from their studies of ^{78,86}Kr fragmentation at intermediate energies [9].

In an earlier experiment we have measured the projectile fragmentation of ^{136}Xe [10], the most neutron-rich stable xenon isotope. In the present experiment the fragmentation of ^{129}Xe was investigated with several questions to be addressed. First the memory effect in the mass region $A > 100$ should be verified by comparison to the ^{136}Xe data. Furthermore, the very neutron-deficient tails of the fragment distributions were to be studied to investigate the production of

nuclei near the proton dripline in the mass region $A \approx 100$.

Apart from the study of isotopic distributions, a further objective was to measure the momentum distributions of the fragments with high precision. This should allow us to get more insight into the underlying reaction mechanism, which is commonly described as a two-step process [11]. In a first collision phase nucleons are abraded from the projectile by individual nucleon-nucleon scattering processes. An excited prefragment is left, which then deexcites by the emission of nucleons and γ rays in an evaporationlike cascade process to form the fragment finally observed. Since models which ignore the specific characteristics of the nucleon-nucleon scattering processes in the first reaction step, the so-called abrasion-ablation models (e.g., Ref. [12], and references therein), are quite successful in describing the isotopic distributions, further observables have to be measured to distinguish between different models. The deexcitation of the prefragments should be governed by an isotropic emission of particles and thus only influence the width of the momentum distributions. In contrast, the mean value of the fragment momentum should be sensitive only to the collision phase. Therefore the clue to disentangle the different reaction steps and their influence on the final fragment formation is a detailed study of the momentum distributions.

In this paper first the experimental procedure will be presented. Then the results will be discussed on a phenomenological basis. A more detailed discussion with a comparison to an intranuclear-cascade model will be given in a forthcoming paper.

II. EXPERIMENTAL PROCEDURE

The experiment was performed at the GSI facility at Darmstadt, Germany. ^{129}Xe ions were accelerated in the heavy-ion synchrotron SIS to an energy of 790A MeV. Spills with intensities of up to 10^8 ions lasting for about 3–4 s with a repetition rate of 1/5 s^{-1} were focussed onto an (803±2) mg/cm^2 aluminum target in front of the fragment separator (FRS) [13]. The experimental setup is sketched in Fig.

*Present address: Physics Division, Argonne National Laboratory, 9700 South Cass Avenue, Argonne, Illinois 60439.
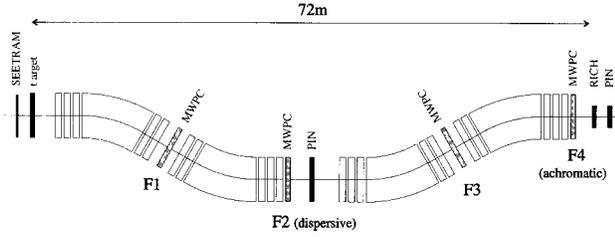
FIG. 1. Experimental setup at the fragment separator FRS. The multiwire proportional counters (MWPC's) at focal points F1 to F4 were only used to tune the separator and were removed from the beam during the actual measurements. The silicon detectors (PIN) and the Čerenkov detector (RICH) were positioned in the momentum-dispersive focus F2 and in the achromatic focus F4, respectively.

1. The primary beam intensity was determined from the current induced by delta electrons in an aluminum converter foil (SEETRAM [14]) in front of the target. This detector had an areal thickness of 9 mg/cm^2 aluminum, thus increasing the total target thickness to 812 mg/cm^2 aluminum. With a total reaction cross section of $\sigma_{total} = 3.5$ b calculated from an empirical parametrization [15] the total reaction rate of the primary beam in this target was 6.3%. Several large-area multiwire proportional counters (MWPC's) were available at the different focal planes. These could be moved into the beam to tune the separator. The projectilelike fragments produced were separated from the beam in the first half of the FRS. In the momentum-dispersive central focal plane (F2) their positions and thus their magnetic rigidities were measured with a segmented silicon detector array. This detector consisted of sixty-four 220 μm thick silicon photodiodes with an active area of 10×10 mm^2. They were arranged into four subsequent layers of 16×1 cm^2, which were shifted against each preceding layer by 2.5 mm in horizontal (bending) direction. This results in a position resolution of ± 1.25 mm, which translates into a momentum resolution of $\Delta p/p = 1.7 \times 10^{-4}$. This detector system also served to determine the nuclear charge by measuring the energy-loss of the fragments. The second half of the separator was tuned such as to produce an achromatic focus in the final focal plane F4, which means that at this focus the fragment positions are independent of their momenta. Here their velocities were measured with a ring-imaging Čerenkov detector [16]. A second silicon detector array behind the Čerenkov detector with an active area of 60×30 mm^2 served as an additional trigger detector.

The SEETRAM beam intensity monitor was calibrated at low beam currents ($\leqslant 2 \times 10^5$ ions/s) by counting individual beam particles with a scintillator which could be moved into the beam. We estimate the error of the beam intensity to be 5–17 %, resulting from both the calibration error and the counting statistics of the SEETRAM current digitizer.

The magnetic dipole fields were measured by Hall probes with an accuracy of $\Delta B = 10^{-4}$ T. The dispersion in the central focal plane F2 was determined to be $D = \Delta x/(\Delta B\rho/B\rho_0) = (74.58 \pm 0.65)$ mm/% by measuring the position of the primary beam for several field settings. With a beam spot of $\Delta x \approx \pm 2.7$ mm at the target and a position resolution of the silicon detector at the central focal plane F2 of $\Delta x = \pm 1.25$ mm this allowed to determine the momentum
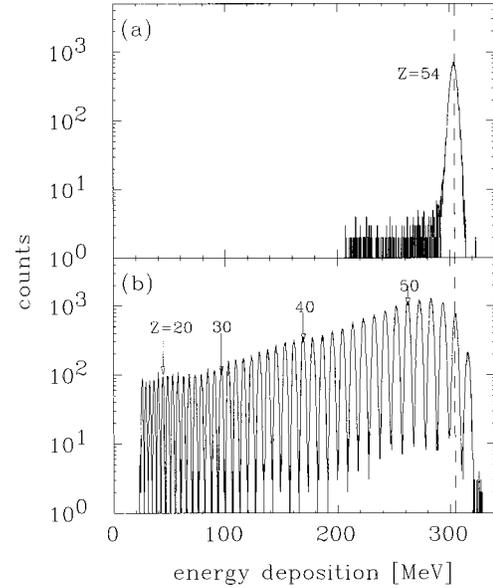
FIG. 2. Response of the silicon detector array at F2. (a): The primary beam with $Z = 54$ was used for calibration. Shown is the response of a single detector chip in one layer. The low-energy tail results from fragments. (b) Charge resolution of the entire detector system for fragments with $B\rho = (10.486 \pm 0.105)$Tm, corresponding to $A/Q \approx (2.24 \pm 0.02)$.

for fragments with known ionic charge with an accuracy of $\Delta|\vec{P}| \approx 60$ MeV/c.

The fragment nuclear charge number Z was determined from a fourfold energy-loss measurement in the silicon detector array at F2. This detector was calibrated with the primary beam for the nuclear charge number $Z = 54$ [Fig. 2(a)]. At this energy 99% of the ions are fully ionized ($Q = Ze$) [17]. Thus this measurement also determines the ionic charge of the fragments.

The velocity resolution achieved with the Čerenkov detector was $\Delta\beta/\beta = 1.8 \times 10^{-3}$ [16]. Together with the magnetic-rigidity and energy-loss measurements, the fragments could be identified with respect to nuclear charge and mass number.

As the spectrometer acceptance is about $\pm 1\%$ in momentum, several field settings were necessary to cover the neutron-deficient area of the nuclear chart in the projectile mass region up to the vicinity of the proton dripline. In addition in one setting we selected fragments that were more neutron-rich than the projectile for comparison with an earlier experiment using a ^{136}Xe beam [10]. The different field settings were each optimized for the transmission of a specific tin isotope.

III. RESULTS

A. Isotope identification

In Fig. 2 an energy-loss spectrum obtained with the silicon detector at F2 is shown. The upper part shows the response of a single diode to the primary beam with $Z = 54$. The low-energy tail in this spectrum results from fragmentation products with magnetic rigidities similar to that of the
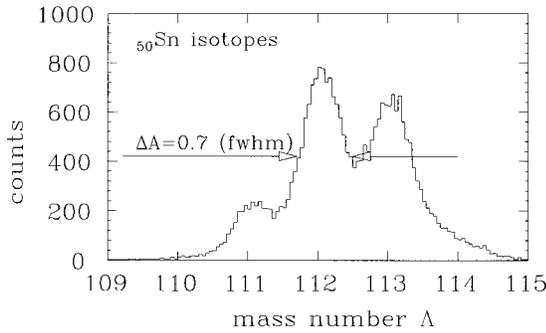
FIG. 3. Mass spectrum for tin isotopes with $B\rho = (10.486 \pm 0.105)$Tm.

beam. The four layers of the Si detector allow a fourfold energy-loss measurement, which further improves the resolution.

The lower part of Fig. 2 shows the response of the entire detector system to fragments measured with the spectrometer setting optimized for the transmission of the isotope ^{112}Sn. The different nuclear charges are clearly resolved. As the fragment velocities are close to the beam velocity, which again is near the minimum-ionizing region, the absolute value of the nuclear charge number can be obtained by direct comparison with the beam spectrum. Applying three-sigma window conditions on this charge spectrum in the further analysis, the probability for misidentification in charge number is below 2%. Neglecting this small ambiguity, integer numbers were assigned to the individual fragments in the subsequent analysis.

For fragments with nuclear charge numbers below $Z = 40$ the different energy losses, compared to the nominal fragment, lead to a horizontal displacement of their foci at the final focal plane F4 which is too large to be accepted by the Čerenkov detector. Therefore only fragments with $Z \geqslant 40$ could be identified. The response of the Čerenkov detector and its analysis are discussed elsewhere [16]. A resulting mass spectrum obtained by combining the charge, velocity, and position measurements is shown in Fig. 3 for tin isotopes. The appearance of mainly three isotopes reflects the spectrometer momentum acceptance of $\pm 1\%$ which corresponds to ± 1 mass unit for isotopes with nuclear mass number $A \approx 100$. The relative intensities of the three tin isotopes in Fig. 3 are dominated by their different transmissions through the spectrometer rather than their production cross sections. The upper part of Fig. 4 shows the measured velocity vs the position at F2 for the same isotopic distribution. This demonstrates that the width of the momentum distributions is of the same order as the spectrometer acceptance and therefore only the central isotope (here ^{112}Sn) is expected to have a transmission near 100%.

B. Determination of cross sections

Individual isotopic cross sections were determined from the number of counts in the projected position spectra such as the ones shown in the bottom part of Fig. 4. This allowed us to determine the ion-optical transmission also. The transmission was derived from the ratio of the measured counts to the area of a fitted Gaussian function folded with a rectangular distribution. The rectangular distribution accounts for
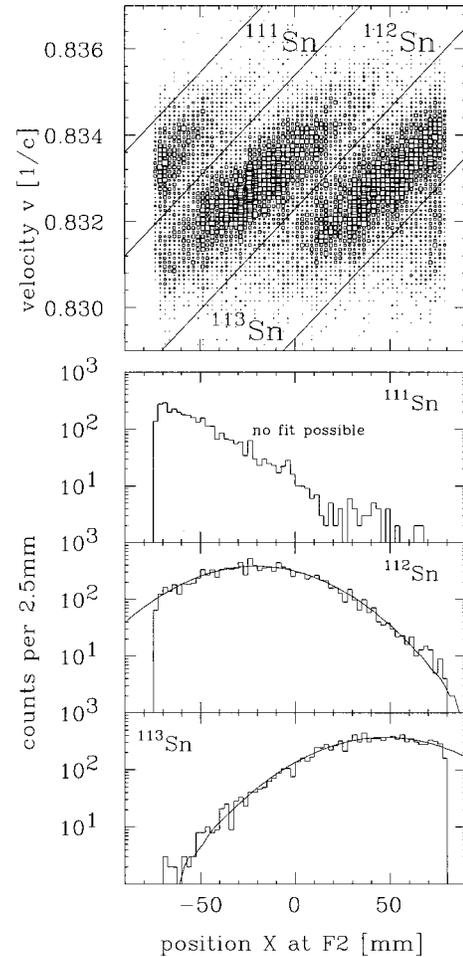
FIG. 4. Top: Measured velocity vs position at the dispersive focus F2 for tin isotopes with $B\rho = (10.486 \pm 0.105)$Tm. Bottom: Projections on the horizontal axis for the three isotopes shown in the top figure. The spectra were fitted by a Gaussian folded with a rectangular distribution. For the isotope ^{111}Sn no reliable fit was possible, but it could be measured with an adjacent field setting.

the different energy losses of projectile and fragment in the target. Its width was fixed and determined from energy loss calculations [18]. As there is no comparable information perpendicular to the bending direction, transmission losses in vertical direction where determined by occasionally starting the data acquisition with the larger MWPC's. The ratio of correlated to uncorrelated events between these detectors and the silicon detector indicated an additional transmission loss of 5%.

The overall efficiency, including ionic charge changes, secondary reactions in the detectors and deadtime was approximately 60%. The experimental errors are dominated by the beam intensity monitor (5–17%) and the transmission determination (10–50%). For isotopes with low transmission no reliable fit of the position distributions was possible (see, e.g., the ^{111}Sn distribution in Fig. 4). But in most cases such isotopes were observed with higher transmission in an adjacent field setting. For isotopes where the distributions could be fitted in two settings, the results agree within the extracted errors. Only for distributions with low statistics, which did not allow a reliable fit, a Monte Carlo simulation [19] of the spectrometer transmission was used. This simulation agreed

TABLE I. Measured cross sections and momentum distributions (average momentum $\langle P \rangle$ and rms width P_{rms} measured in the projectile frame) for the respective fragments formed in the reaction of 790A MeV ^{129}Xe + ^{27}Al. For some isotopes only a cross section is given, as no reliable fit of the momentum distribution was possible.

El.	Z	A	cross section [b]	$\langle P \rangle$ [MeV/c]	P_{rms} [MeV/c]	El.	Z	A	cross section [b]	$\langle P \rangle$ [MeV/c]	P_{rms} [MeV/c]
Cs	55	129	$(8.53\pm0.80)\times10^{-4}$	-177 ± 90	75 ± 11	Sb	51	125	$(1.32\pm0.16)\times10^{-4}$	-82 ± 85	175 ± 18
Cs	55	128	$(2.29\pm0.19)\times10^{-3}$	-161 ± 41	91 ± 10	Sb	51	119	$(7.89\pm0.54)\times10^{-3}$	-168 ± 52	254 ± 28
Cs	55	127	$(4.18\pm0.30)\times10^{-3}$	-168 ± 86	104 ± 11	Sb	51	118	$(1.09\pm0.07)\times10^{-2}$	-189 ± 61	297 ± 32
Cs	55	126	$(3.83\pm0.36)\times10^{-3}$	-196 ± 43	124 ± 13	Sb	51	117	$(1.30\pm0.11)\times10^{-2}$	-213 ± 50	282 ± 30
Cs	55	125	$(3.62\pm0.34)\times10^{-3}$	-207 ± 76	144 ± 16	Sb	51	116	$(1.43\pm0.12)\times10^{-2}$	-217 ± 60	304 ± 32
Cs	55	124	$(2.04\pm0.39)\times10^{-3}$	-274 ± 49	140 ± 21	Sb	51	115	$(1.49\pm0.26)\times10^{-2}$	-319 ± 48	296 ± 34
Cs	55	123	$(1.46\pm0.28)\times10^{-3}$	-298 ± 77	180 ± 33	Sb	51	114	$(1.30\pm0.23)\times10^{-2}$	-310 ± 70	316 ± 40
Cs	55	122	$(6.77\pm0.74)\times10^{-4}$	-282 ± 63	182 ± 34	Sb	51	113	$(7.94\pm0.59)\times10^{-3}$	-306 ± 50	321 ± 36
Cs	55	121	$(2.39\pm0.28)\times10^{-4}$	-302 ± 87	220 ± 58	Sb	51	112	$(5.21\pm0.41)\times10^{-3}$	-303 ± 69	333 ± 49
Cs	55	120	$(1.19\pm1.20)\times10^{-4}$			Sb	51	111	$(1.40\pm0.18)\times10^{-3}$	-405 ± 74	370 ± 66
Cs	55	119	$(1.36\pm0.69)\times10^{-5}$			Sb	51	110	$(5.45\pm1.05)\times10^{-4}$	-368 ± 182	388 ± 195
Cs	55	118	$(6.06\pm3.69)\times10^{-6}$			Sb	51	109	$(6.84\pm1.14)\times10^{-5}$		
Xe	54	126	$(3.12\pm0.24)\times10^{-2}$	-96 ± 54	112 ± 11	Sb	51	108	$(1.02\pm0.83)\times10^{-5}$		
Xe	54	125	$(2.33\pm0.18)\times10^{-2}$	-106 ± 58	144 ± 14	Sn	50	124	$(4.65\pm0.65)\times10^{-6}$	-127 ± 61	188 ± 33
Xe	54	124	$(1.98\pm0.16)\times10^{-2}$	-159 ± 58	161 ± 16	Sn	50	123	$(2.70\pm0.32)\times10^{-5}$	-106 ± 56	211 ± 23
Xe	54	123	$(1.54\pm0.12)\times10^{-2}$	-162 ± 53	179 ± 18	Sn	50	122	$(4.98\pm1.07)\times10^{-5}$		
Xe	54	122	$(9.38\pm1.71)\times10^{-3}$	-248 ± 61	185 ± 21	Sn	50	117	$(4.44\pm0.34)\times10^{-3}$	-196 ± 77	278 ± 42
Xe	54	121	$(6.11\pm1.15)\times10^{-3}$	-255 ± 53	201 ± 25	Sn	50	116	$(5.79\pm0.40)\times10^{-3}$	-174 ± 44	285 ± 33
Xe	54	120	$(3.88\pm0.28)\times10^{-3}$	-251 ± 73	232 ± 31	Sn	50	115	$(8.73\pm0.77)\times10^{-3}$	-244 ± 70	316 ± 39
Xe	54	119	$(1.28\pm0.11)\times10^{-3}$	-286 ± 55	237 ± 35	Sn	50	114	$(1.16\pm0.09)\times10^{-2}$	-215 ± 44	304 ± 32
Xe	54	118	$(4.21\pm0.81)\times10^{-4}$			Sn	50	113	$(1.20\pm0.23)\times10^{-2}$	-300 ± 69	326 ± 45
Xe	54	117	$(7.17\pm1.74)\times10^{-5}$			Sn	50	112	$(1.32\pm0.23)\times10^{-2}$	-307 ± 53	334 ± 41
Xe	54	116	$(1.18\pm1.45)\times10^{-5}$			Sn	50	111	$(1.14\pm0.09)\times10^{-2}$	-310 ± 65	357 ± 43
Xe	54	115	$(3.08\pm2.75)\times10^{-6}$			Sn	50	110	$(8.22\pm0.53)\times10^{-3}$	-314 ± 53	340 ± 41
I	53	124	$(2.23\pm0.14)\times10^{-2}$	-118 ± 74	184 ± 18	Sn	50	109	$(2.88\pm0.36)\times10^{-3}$	-429 ± 63	327 ± 52
I	53	123	$(2.43\pm0.15)\times10^{-2}$	-12 ± 42	193 ± 19	Sn	50	108	$(1.27\pm0.17)\times10^{-3}$	-432 ± 72	359 ± 101
I	53	122	$(1.93\pm0.16)\times10^{-2}$	-161 ± 78	215 ± 22	Sn	50	107	$(2.40\pm0.22)\times10^{-4}$	-365 ± 107	432 ± 89
I	53	121	$(2.07\pm0.17)\times10^{-2}$	-176 ± 40	229 ± 23	Sn	50	106	$(3.80\pm0.51)\times10^{-5}$		
I	53	120	$(1.40\pm0.25)\times10^{-2}$	-258 ± 80	227 ± 28	Sn	50	105	$(4.23\pm0.95)\times10^{-6}$		
I	53	119	$(1.16\pm0.20)\times10^{-2}$	-269 ± 43	245 ± 28	Sn	50	104	$(5.77\pm3.61)\times10^{-7}$		
I	53	118	$(7.23\pm1.57)\times10^{-3}$	-259 ± 98	277 ± 42	Sn	50	102	$(1.12\pm2.00)\times10^{-9}$		
I	53	117	$(2.45\pm0.24)\times10^{-3}$	-289 ± 43	257 ± 32	In	49	122	$(1.50\pm0.29)\times10^{-6}$		
I	53	116	$(1.05\pm0.21)\times10^{-3}$	-230 ± 108	220 ± 54	In	49	121	$(8.86\pm1.15)\times10^{-6}$	-135 ± 46	225 ± 33
I	53	115	$(2.85\pm0.38)\times10^{-4}$	-366 ± 102	306 ± 95	In	49	120	$(2.41\pm0.32)\times10^{-5}$	-110 ± 94	257 ± 36
I	53	114	$(4.19\pm4.50)\times10^{-5}$			In	49	115	$(1.80\pm0.26)\times10^{-3}$		
I	53	113	$(7.20\pm8.80)\times10^{-6}$			In	49	114	$(3.53\pm0.25)\times10^{-3}$		
Te	52	128	$(1.65\pm0.49)\times10^{-5}$	-98 ± 55	94 ± 11	In	49	113	$(4.91\pm0.39)\times10^{-3}$		
Te	52	127	$(3.67\pm0.55)\times10^{-4}$			In	49	112	$(8.12\pm0.66)\times10^{-3}$		
Te	52	122	$(1.07\pm0.11)\times10^{-2}$	-181 ± 95	190 ± 23	In	49	111	$(1.09\pm0.20)\times10^{-2}$		
Te	52	121	$(1.40\pm0.09)\times10^{-2}$	-148 ± 40	226 ± 23	In	49	110	$(1.03\pm0.18)\times10^{-2}$		
Te	52	120	$(1.65\pm0.11)\times10^{-2}$	-158 ± 81	251 ± 27	In	49	109	$(1.25\pm0.17)\times10^{-2}$	-354 ± 89	374 ± 52
Te	52	119	$(1.65\pm0.13)\times10^{-2}$	-195 ± 39	248 ± 25	In	49	108	$(8.42\pm0.60)\times10^{-3}$	-333 ± 45	367 ± 42
Te	52	118	$(1.77\pm0.15)\times10^{-2}$	-201 ± 79	273 ± 29	In	49	107	$(5.16\pm0.65)\times10^{-3}$	-442 ± 93	386 ± 64
Te	52	117	$(1.39\pm0.24)\times10^{-2}$	-276 ± 41	268 ± 30	In	49	106	$(1.77\pm0.22)\times10^{-3}$	-356 ± 77	412 ± 77
Te	52	116	$(1.10\pm0.20)\times10^{-2}$	-276 ± 88	288 ± 42	In	49	105	$(5.61\pm0.45)\times10^{-4}$	-391 ± 97	425 ± 69
Te	52	115	$(6.01\pm0.50)\times10^{-3}$	-292 ± 42	265 ± 30	In	49	104	$(1.00\pm0.10)\times10^{-4}$	-295 ± 129	478 ± 143
Te	52	114	$(3.13\pm0.30)\times10^{-3}$	-279 ± 84	274 ± 48	In	49	103	$(1.04\pm0.18)\times10^{-5}$		
Te	52	113	$(6.07\pm0.84)\times10^{-4}$	-380 ± 79	336 ± 66	In	49	102	$(0.43\pm1.92)\times10^{-5}$		
Te	52	112	$(2.97\pm1.09)\times10^{-4}$			Cd	48	119	$(2.02\pm0.31)\times10^{-6}$	-172 ± 88	270 ± 106
Te	52	111	$(2.42\pm0.96)\times10^{-5}$			Cd	48	118	$(9.16\pm1.19)\times10^{-6}$	-137 ± 65	265 ± 44
Te	52	110	$(2.01\pm3.91)\times10^{-5}$			Cd	48	112	$(1.94\pm0.15)\times10^{-3}$		
Sb	51	127	$(2.46\pm2.25)\times10^{-7}$			Cd	48	111	$(2.96\pm0.22)\times10^{-3}$		
Sb	51	126	$(1.72\pm0.27)\times10^{-5}$	-89 ± 41	151 ± 17						

TABLE I. (*Continued*).

El.	Z	A	cross section [b]	$\langle P \rangle$ [MeV/c]	P_{rms} [MeV/c]	El.	Z	A	cross section [b]	$\langle P \rangle$ [MeV/c]	P_{rms} [MeV/c]
Cd	48	110	$(7.28\pm0.63)\times10^{-3}$			Rh	45	94	$(2.37\pm0.26)\times10^{-5}$	-377 ± 161	506 ± 204
Cd	48	109	$(9.57\pm2.45)\times10^{-3}$			Ru	44	103	$(4.46\pm0.69)\times10^{-4}$		
Cd	48	108	$(9.73\pm1.72)\times10^{-3}$			Ru	44	102	$(6.89\pm0.61)\times10^{-4}$		
Cd	48	107	$(1.10\pm0.21)\times10^{-2}$	-370 ± 144	394 ± 70	Ru	44	101	$(1.67\pm0.35)\times10^{-3}$		
Cd	48	106	$(9.17\pm0.68)\times10^{-3}$	-353 ± 43	404 ± 47	Ru	44	100	$(2.80\pm0.25)\times10^{-3}$		
Cd	48	105	$(9.18\pm1.03)\times10^{-3}$	-492 ± 102	360 ± 63	Ru	44	99	$(5.28\pm0.94)\times10^{-3}$		
Cd	48	104	$(3.22\pm0.38)\times10^{-3}$	-407 ± 61	413 ± 63	Ru	44	98	$(6.06\pm1.17)\times10^{-3}$	-521 ± 127	400 ± 81
Cd	48	103	$(1.04\pm0.10)\times10^{-3}$	-418 ± 100	426 ± 63	Ru	44	97	$(7.41\pm0.49)\times10^{-3}$	-358 ± 51	447 ± 63
Cd	48	102	$(2.17\pm0.17)\times10^{-4}$	-293 ± 66	380 ± 67	Ru	44	96	$(7.27\pm0.90)\times10^{-3}$	-453 ± 109	455 ± 82
Cd	48	101	$(2.56\pm0.33)\times10^{-5}$	-402 ± 55	467 ± 48	Ru	44	95	$(3.03\pm0.73)\times10^{-3}$	-402 ± 93	459 ± 99
Cd	48	100	$(2.75\pm0.92)\times10^{-6}$			Ru	44	94	$(1.47\pm0.10)\times10^{-3}$	-404 ± 63	499 ± 70
Ag	47	117	$(1.62\pm0.33)\times10^{-6}$	-256 ± 252	296 ± 282	Ru	44	93	$(2.24\pm0.24)\times10^{-4}$	-525 ± 197	491 ± 100
Ag	47	116	$(5.30\pm0.74)\times10^{-6}$	-181 ± 77	256 ± 93	Ru	44	92	$(3.14\pm0.30)\times10^{-5}$	-385 ± 151	559 ± 218
Ag	47	115	$(1.87\pm0.27)\times10^{-5}$	-112 ± 164	300 ± 87	Tc	43	100	$(4.23\pm0.45)\times10^{-4}$		
Ag	47	110	$(8.55\pm1.00)\times10^{-4}$			Tc	43	99	$(9.91\pm1.27)\times10^{-4}$		
Ag	47	109	$(2.23\pm0.16)\times10^{-3}$			Tc	43	98	$(2.01\pm0.19)\times10^{-3}$		
Ag	47	108	$(3.76\pm0.34)\times10^{-3}$			Tc	43	97	$(4.39\pm0.79)\times10^{-3}$		
Ag	47	107	$(5.77\pm0.48)\times10^{-3}$			Tc	43	96	$(5.00\pm0.91)\times10^{-3}$		
Ag	47	106	$(8.24\pm1.45)\times10^{-3}$			Tc	43	95	$(7.24\pm0.48)\times10^{-3}$	-365 ± 53	437 ± 64
Ag	47	105	$(9.33\pm1.65)\times10^{-3}$			Tc	43	94	$(5.50\pm0.51)\times10^{-3}$	-559 ± 120	429 ± 83
Ag	47	104	$(9.06\pm0.64)\times10^{-3}$	-378 ± 47	400 ± 48	Tc	43	93	$(4.81\pm0.57)\times10^{-3}$	-394 ± 76	485 ± 92
Ag	47	103	$(7.62\pm0.70)\times10^{-3}$	-353 ± 115	447 ± 80	Tc	43	92	$(1.78\pm0.12)\times10^{-3}$	-451 ± 70	478 ± 66
Ag	47	102	$(4.13\pm0.48)\times10^{-3}$	-401 ± 60	444 ± 68	Tc	43	91	$(3.50\pm0.37)\times10^{-4}$	-316 ± 140	493 ± 125
Ag	47	101	$(1.86\pm0.24)\times10^{-3}$	-429 ± 118	447 ± 66	Tc	43	90	$(3.77\pm0.35)\times10^{-5}$	-403 ± 133	531 ± 178
Ag	47	100	$(4.43\pm0.36)\times10^{-4}$	-337 ± 66	484 ± 83	Mo	42	98	$(2.41\pm0.31)\times10^{-4}$		
Ag	47	99	$(5.46\pm0.51)\times10^{-5}$	-427 ± 201	480 ± 124	Mo	42	97	$(5.20\pm0.57)\times10^{-4}$		
Ag	47	98	$(6.14\pm1.17)\times10^{-6}$			Mo	42	96	$(1.43\pm0.14)\times10^{-3}$		
Pd	46	114	$(1.11\pm0.20)\times10^{-6}$			Mo	42	95	$(2.47\pm0.48)\times10^{-3}$		
Pd	46	113	$(4.64\pm0.71)\times10^{-6}$	-208 ± 155	337 ± 160	Mo	42	94	$(4.99\pm0.90)\times10^{-3}$		
Pd	46	112	$(8.87\pm3.64)\times10^{-6}$			Mo	42	93	$(6.10\pm0.44)\times10^{-3}$	-411 ± 78	464 ± 81
Pd	46	107	$(1.09\pm0.09)\times10^{-3}$			Mo	42	92	$(6.52\pm0.56)\times10^{-3}$	-345 ± 137	479 ± 103
Pd	46	106	$(2.27\pm0.26)\times10^{-3}$			Mo	42	91	$(5.32\pm0.63)\times10^{-3}$	-404 ± 80	473 ± 111
Pd	46	105	$(4.04\pm0.34)\times10^{-3}$			Mo	42	90	$(1.93\pm0.15)\times10^{-3}$	-479 ± 89	497 ± 73
Pd	46	104	$(6.77\pm1.23)\times10^{-3}$			Mo	42	89	$(4.37\pm0.34)\times10^{-4}$	-328 ± 118	529 ± 130
Pd	46	103	$(8.13\pm1.43)\times10^{-3}$			Mo	42	88	$(7.30\pm0.59)\times10^{-5}$	-422 ± 132	546 ± 165
Pd	46	102	$(9.09\pm0.63)\times10^{-3}$	-370 ± 68	431 ± 61	Nb	41	96	$(1.67\pm0.72)\times10^{-4}$		
Pd	46	101	$(8.30\pm0.59)\times10^{-3}$	-356 ± 83	445 ± 66	Nb	41	95	$(2.75\pm0.32)\times10^{-4}$		
Pd	46	100	$(5.73\pm0.67)\times10^{-3}$	-438 ± 59	432 ± 62	Nb	41	94	$(9.47\pm1.03)\times10^{-4}$		
Pd	46	99	$(2.13\pm0.28)\times10^{-3}$	-331 ± 171	441 ± 137	Nb	41	93	$(1.80\pm0.18)\times10^{-3}$		
Pd	46	98	$(7.14\pm0.55)\times10^{-4}$	-369 ± 58	495 ± 76	Nb	41	92	$(3.83\pm0.69)\times10^{-3}$		
Pd	46	97	$(1.02\pm0.09)\times10^{-4}$	-473 ± 167	460 ± 99	Nb	41	91	$(5.56\pm0.42)\times10^{-3}$	-427 ± 124	476 ± 110
Pd	46	96	$(1.11\pm0.14)\times10^{-5}$			Nb	41	90	$(6.14\pm0.48)\times10^{-3}$	-387 ± 112	523 ± 139
Rh	45	112	$(8.78\pm21.45)\times10^{-7}$			Nb	41	89	$(5.56\pm0.65)\times10^{-3}$	-458 ± 70	470 ± 92
Rh	45	111	$(2.14\pm0.32)\times10^{-6}$			Nb	41	88	$(1.75\pm0.27)\times10^{-3}$	-502 ± 113	507 ± 79
Rh	45	110	$(5.23\pm0.82)\times10^{-6}$			Nb	41	87	$(5.70\pm0.44)\times10^{-4}$	-389 ± 100	542 ± 129
Rh	45	105	$(5.74\pm0.55)\times10^{-4}$			Nb	41	86	$(1.01\pm0.09)\times10^{-4}$	-415 ± 155	565 ± 166
Rh	45	104	$(1.22\pm0.10)\times10^{-3}$			Zr	40	93	$(1.61\pm0.24)\times10^{-4}$		
Rh	45	103	$(2.85\pm0.25)\times10^{-3}$			Zr	40	92	$(4.58\pm0.76)\times10^{-4}$		
Rh	45	102	$(3.47\pm0.33)\times10^{-3}$			Zr	40	91	$(1.16\pm0.13)\times10^{-3}$		
Rh	45	101	$(6.63\pm1.17)\times10^{-3}$			Zr	40	90	$(3.49\pm0.65)\times10^{-3}$		
Rh	45	100	$(8.15\pm0.64)\times10^{-3}$	-395 ± 105	424 ± 68	Zr	40	89	$(4.45\pm0.45)\times10^{-3}$	-540 ± 141	411 ± 102
Rh	45	99	$(7.89\pm0.53)\times10^{-3}$	-357 ± 62	454 ± 65	Zr	40	88	$(5.88\pm0.43)\times10^{-3}$	-330 ± 71	497 ± 111
Rh	45	98	$(6.38\pm0.76)\times10^{-3}$	-449 ± 76	436 ± 68	Zr	40	^{87}	$(5.81\pm0.71)\times10^{-3}$	-463 ± 105	501 ± 115
Rh	45	97	$(3.02\pm0.37)\times10^{-3}$	-407 ± 150	483 ± 135	Zr	40	86	$(2.24\pm0.23)\times10^{-3}$	-561 ± 127	491 ± 80
Rh	45	96	$(1.06\pm0.07)\times10^{-3}$	-405 ± 56	480 ± 69	Zr	40	85	$(7.14\pm0.53)\times10^{-4}$	-419 ± 71	505 ± 103
Rh	45	95	$(1.50\pm0.14)\times10^{-4}$	-465 ± 198	490 ± 112						

with the measured transmissions within about 5%.

Cross sections down to 1 nb could be determined in the mass region $80 < A < 129$ with nuclear charge numbers Z from 40 to 55. All derived cross sections are given in Table I. The charge-pickup process leading to fragments with $Z_{frag} = 55$ has been discussed in a separate paper [20].

C. Momentum distributions

The average momentum and the width of the fragment momentum distributions were determined from the position spectra (Fig. 4) assuming a Gaussian momentum distribution folded with a rectangular distribution as described in Sec. III B. Both quantities were transformed into the projectile restframe. The velocity change of projectile and fragment due to energy loss in the target was determined by energy loss calculations [18], which have been shown to be accurate to about 2% [13]. Due to the large fragment momentum in the laboratory frame the contribution of transverse momentum components to the total momentum is smaller than the spectrometer resolution. Thus the experiment was only sensitive to the longitudinal (in beam direction) momentum change. Transverse components should in principal be measurable by determining the fragment angular distributions, but were not achievable with the present layout of the silicon detector used in the central focal plane.

The field measurement, the position measurement and the calibration of the dispersion contribute to the error with $\Delta P/P = 1 \times 10^{-4}, 4 \times 10^{-4}$, and 8.8×10^{-5}, respectively. Additional contributions arise from uncertainties in the fitting procedure, i.e., for distributions with low statistics or low transmission. The results are summarized in Table I.

IV. DISCUSSION

A. Cross sections

Representative examples of isotopic distributions for the elements of Te, Sn, and Rh are shown in Fig. 5. They exhibit the typical Gaussian-like shapes, where the slope of the neutron-rich tail is less steep than that of the neutron-deficient side. In general these distributions are reproduced by the empirical parametrization EPAX [3] (full line) with respect to the position of their maxima and their shape. The most significant deviations occur for neutron-rich fragments with masses close to that of the projectile. The production of these fragments should be governed by the "cold" removal of protons, because excitation of the projectile dominantly leads to neutron evaporation, which is not hampered by the Coulomb barrier. Therefore a parametrization, which mainly has been fitted to spallation data, is not expected to describe these specific reaction channels. This had already been observed in other experiments [21], including our previous measurement with the ^{136}Xe projectile [10] (the latter is shown in Fig. 5 with the circled symbols and dashed lines). Aside from this deficiency the shift of the isotopic distributions is described satisfactorily. However, a direct comparison of the two projectiles is only possible for the neutron-rich tail due to experimental constraints in the ^{136}Xe experiment. As indicated by the arrows in Fig. 5, the excess of seven neutrons for the ^{136}Xe projectile is fully preserved for fragments close to the projectile (tellurium isotopes in Fig. 5), and even for fragments that have lost as much as 20

nucleons a shift of the neutron-rich tail of the isotopic distribution by four mass units is clearly visible (rhodium isotopes in Fig. 5). Up to now this memory effect has only been observed for lighter nuclei [5–7]. Therefore our data corroborate the quantitative description of the "memory effect" contained in EPAX for heavier projectiles.

Particular attention should be paid to the neutron-deficient tin isotopes, where due to the experimental procedure (the separator was always optimized for the transmission of a tin isotope) the lowest cross sections could be measured. The slope of the distribution seems to differ significantly from the EPAX parametrization, a fact that has also been observed for neutron-deficient isotopes produced in the fragmentation of ^{58}Ni projectiles [22]. These observations, and the memory effect, which is also predicted for neutron-deficient projectiles, opens up the prospect to produce the doubly magic nucleus ^{100}Sn by fragmentation of ^{124}Xe, which is the most neutron-deficient xenon isotope available as a projectile. In the meantime this experiment was performed successfully and results have been presented in Refs. [23–25].

B. Longitudinal momentum distributions

Figure 6 shows the measured widths of the fragment momentum distributions in the projectile restframe. In previous studies, authors have compared measured momentum widths (see, e.g., Refs. [26,27]) to the predictions of the Goldhaber model [28]. This "sudden break-up" model predicts the momentum width $\sigma_\parallel$ of a break-up residue (a *prefragment* in our terminology, see Sec. I) with mass A_{pf} to obey the equation

$$\sigma_{P_\parallel} = \sigma_0 \sqrt{\frac{A_{pf}(A_{proj} - A_{pf})}{A_{proj} - 1}}, \qquad (4.1)$$

where $\sigma_0 = \sqrt{1/5} P_{Fermi}$. Here $P_\parallel$ is the longitudinal momentum of the fragments in the projectile restframe, P_{Fermi} the Fermi momentum of nucleons in the projectile, and A_{proj} and A_{pf} the mass number of the projectile and prefragment, respectively. A numerical value of $P_{Fermi} = 260$ MeV/c, can be taken from quasielastic electron scattering data [29].

Since in our experiment we mainly observe fragments which are produced by evaporation cascades from the prefragments, we cannot expect their momentum widths to follow Eq. (4.1). Consequently, the Goldhaber prediction (dashed line in Fig. 6) clearly disagrees with the data. Only in cases where a surviving prefragment can be observed (e.g., proton-removal channels in the fragmentation of neutron-rich projectiles, Refs. [21,30]) good agreement with the Goldhaber model is observed.

The full line in Fig. 6 shows an empirical parametrization,

$$\sigma_{P_\parallel} \approx 87 \ \text{MeV}/c \ \sqrt{A_{proj} - A_{frag}}, \qquad (4.2)$$

which was derived from a large compilation of available experimental data [31] and gives a quite adequate representation of our measured data.

The above-mentioned compilation [31] also gives a parametrization of the mean longitudinal momentum $\langle \tilde{P}_\parallel \rangle = \Delta A 8$ MeV/c, where the definition
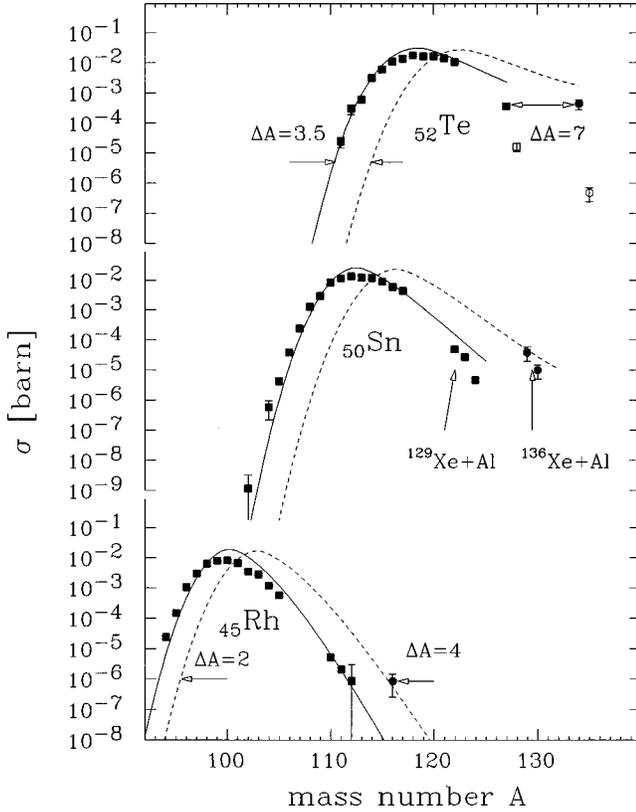
FIG. 5. Measured production cross sections for 760A MeV ^{136}Xe+Al ([10], circles) and 790A MeV ^{129}Xe+Al (this work, squares) compared to the EPAX parametrization [3]. Note that the formation of the most neutron-rich tellurium isotopes (marked with open symbols) requires charge exchange reactions during fragment formation, as $\Delta A = 1$ but $\Delta Z = 2$.

$$\langle \widetilde{P}_\parallel \rangle \equiv m_{\mathrm{proj}} c \langle \beta_\parallel \rangle \frac{\beta \gamma}{\gamma + 1}, \tag{4.3}$$

was used. Here $\langle \beta_\parallel \rangle$ is the average fragment velocity in the projectile restframe, β and γ are the velocity of the projectile and its Lorentz factor, respectively. Thus $\langle \widetilde{P}_\parallel \rangle$ represents the fragment velocity distribution rather than the momentum distribution. It has been pointed out that under certain assumptions $\langle \widetilde{P}_\parallel \rangle$ may be a measure of the excitation energy [31] of the projectile or prefragment. We use this expression for the "average momentum" to compare our data to the systematics in Fig. 7.

In general the slope of the data is reproduced by the parametrization (solid line in Fig. 7), however, there are significant deviations for the individual data points. The best agreement is obtained for the most neutron-rich fragments measured, indicated by open symbols in Fig. 7. The clue for an explanation of this behavior is the origin of the parametrization. Most of the data referred to in Ref. [31] were obtained in target fragmentation experiments. Thus only isotopes with lifetimes sufficiently long to be detected with radiochemical methods could be identified. This restricts the accessible area of the nuclear chart to a region close to the line of β-stability. In contrast, most of our data are for more neutron-deficient nuclei. More neutron-deficient nuclei require longer evaporation chains, on average, and conse-

quently higher excitation energies of the corresponding prefragments, which is in turn related to a stronger slowing-down to convert kinetic energy into excitation energy.

To illustrate this in more detail, we plot in the upper part of Fig. 8 the quantity $\langle \widetilde{P}_\parallel \rangle$ for four isobaric distributions. The full line represents the prediction from the systematics, $\langle \widetilde{P}_\parallel \rangle = \Delta A 8$ MeV/c [31], which is a constant in isobaric chains. Clearly visible is an increasing "momentum transfer" for the more neutron-deficient isobars. This corroborates our interpretation given above that those fragments are formed via higher excitation energies of the corresponding prefragments and subsequent emission of neutrons. In contrast to that neutron-rich fragments have to be formed with low excitation energies, because excitation of the prefragment leads preferably to the emission of neutrons. The same

FIG. 6. Width parameters of the longitudinal momentum distributions. For clarity only one typical error bar is shown for each mass. For individual errors see Table I. Full line: Empirical parametrization by Morrissey [31]. Dashed line: Goldhaber model [28] (see text).
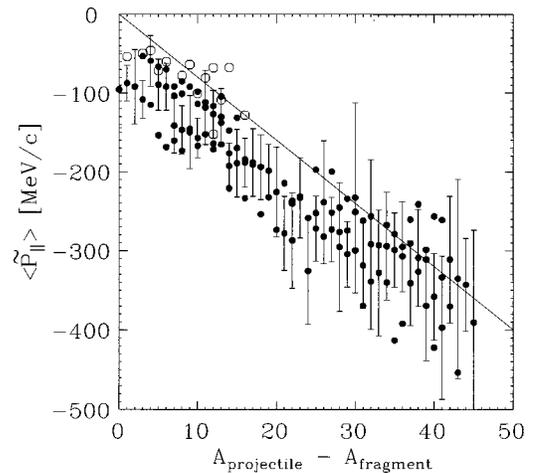
FIG. 7. Mean longitudinal "momentum" compared with the systematic from Morrissey [31]. (Note that $\langle \widetilde{P}_\parallel \rangle$ is not the real fragment momentum but its mean velocity multiplied with a constant factor. For details see text.) Open circles denote fragments measured in the most neutron rich setting. For clarity only one typical error bar is shown for each mass. For individual errors see Table I.
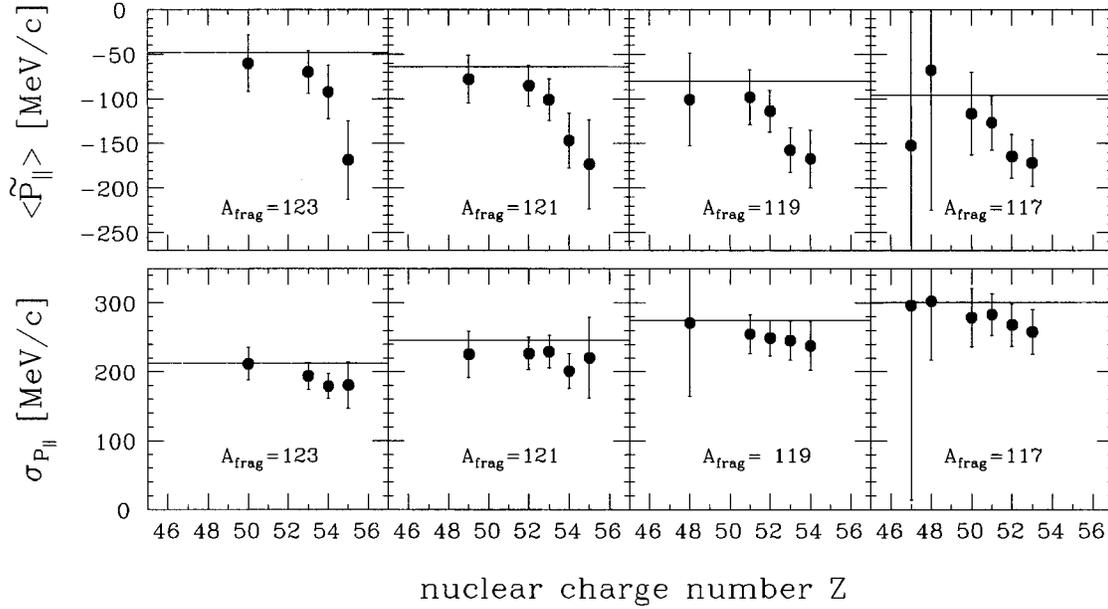
FIG. 8. Isobaric distributions. (Note that $\langle \widetilde{P}_\parallel \rangle$ is not the real fragment momentum but its mean velocity multiplied with a constant factor. For details see text.) The full lines show the empirical parametrizations by Morrissey [31].

conclusion has been reached by Donzaud *et al.* [32] from a correlation of fragment longitudinal momenta with charged-particle multiplicities.

The lower part of Fig. 8 shows the widths of the momentum distributions for the same four isobaric chains. In contrast to the ''average momentum'' they do not exhibit such a significant dependence on the neutron-to-proton ratio. It seems that the more neutron-deficient fragments have slightly narrower momentum distributions. This is what one would expect from the above discussion of the momentum transfer. The higher the excitation energy, the more nucleons will be emitted during the deexcitation phase. Assuming the Goldhaber model still holds for the temporarily formed pre-fragments after the collision phase, the longitudinal root-mean-square momentum per abraded nucleon is approximately $P_{\parallel\mathrm{rms}} \approx \sqrt{1/5} P_{\mathrm{Fermi}} = 116$ MeV/c [see Eq. (4.1)]. This is much larger than the contribution from the evaporation of nucleons: the emission of a nucleon with mass m_N and kinetic energy of $E_{\mathrm{kin}} \approx 2$ MeV results in $P_{\parallel\mathrm{rms}} = \sqrt{1/3}\sqrt{2m_N E_{\mathrm{kin}}} \approx 35$ MeV/c. Thus an increasing contribution of the evaporation phase to the observed mass-loss leads to narrower momentum distributions than expected from the Goldhaber model. This is corroborated by the observation that the momentum distribution of fragments that only have lost protons [21,30] are satisfactorily described by the Gold-haber formalism as discussed above.

V. SUMMARY

We have measured cross sections for projectilelike fragments produced in the reaction $^{129}\mathrm{Xe} + {}^{27}\mathrm{Al}$ at an incident

energy of 790A MeV. A comparison of the isotopic distributions with those of neutron-rich fragments observed in the fragmentation of $^{136}\mathrm{Xe}$ projectiles reveals a dependence of the production yields on the neutron-to-proton ratio of the incident projectile. This so-called ''memory effect'' has only been observed so far for lighter projectiles. The very neutron-deficient tails of the isotopic distributions indicate that production cross sections for nuclei close to the proton dripline where underestimated up to now. For most of the identified fragments the longitudinal momentum distributions were determined. They exhibit a behavior in isobaric chains, which is consistent with the assumption that neutron-deficient fragments are formed from prefragments with higher excitation energies and consequently larger contributions from the subsequent evaporation cascade to the observed mass loss. This set of data now allows a detailed comparison with microscopic descriptions, such as intra-nuclear cascade models, which should allow a more quantitative insight into the underlying reaction mechanism. This will be presented in a forthcoming paper.

[1] H. Geissel, G. Mdunzenberg, and K. Riisager, Annu. Rev. Nucl. Sci. **45**, 163 (1995).

[2] G. Rudstram, Z. Naturforsch. A **21**, 1027 (1966).

[3] K. Sümmerer, W. Brüchle, D. J. Morrissey, M. Schädel, B. Szweryn, and Y. Weifan, Phys. Rev. C **42**, 2546 (1990).

[4] L. Sihver, C. H. Tsao, R. Silberberg, T. Kanai, and A. F.

Barghouty, Phys. Rev. C **47**, 1225 (1993).

 [5] G. D. Westfall, T. J. M. Symons, D. E. Greiner, H. H. Heck-mann, P. J. Lindstrom, J. Mahoney, A. C. Shotter, D. K. Scott, H. J. Crawford, C. McParland, T. C. Awes, C. K. Gelbke, and J. M. Kidd, Phys. Rev. Lett. **43**, 1859 (1979).

 [6] N. T. Porile and L. B. Church, Phys. Rev. **133**, B310 (1964).

 [7] T. H. Ku and P. J. Karol, Phys. Rev. C **16**, 1984 (1977).

 [8] M. Weber, C. Donzuad, J. P. Dufour, H. Geissel, A. Grewe, D. Guillemaud-Mueller, H. Keller, M. Lewitowicz, A. Magel, A. C. Mueller, G. Münzenberg, F. Nickel, M. Pfützner, A. Piechaczek, M. Pravikoff, E. Roeckl, K. Rykaczewski, M. G. Saint-Laurent, I. Schall, C. Stephan, K. Sümmerer, L. Tassan-Got, D. J. Vieira, and B. Voss, Z. Phys. A **343**, 67 (1992).

 [9] R. Pfaff, D. J. Morrissey, W. Benenson, M. Fauerbach, M. Hellström, C. F. Powell, B. M. Sherrill, M. Steiner, and J. A. Winger, Phys. Rev. C **53**, 1753 (1996).

[10] J. Friese, H.-J. Körner, J. Reinhold, R. Schneider, H. Trieb, K. Zeitelhack, B. Blank, T. Brohm, Y. Fujita, H. Geissel, W. König, G. Münzenberg, F. Nickel, M. Pfützner, K. Rykaczew-wski, I. Schall, D. Schardt, A. Schröter, M. Steiner, K. Süm-merer, B. Voss, and J. Weckenmann, Nucl. Phys. **A553**, 735c (1993).

[11] R. Serber, Phys Rev. **72**, 1114 (1947).

[12] J.-J. Gaimard and K.-H. Schmidt, Nucl. Phys. **A531**, 709 (1991).

[13] H. Geissel, P. Armbruster, K. H. Behr, A. Brünle, K. Burkard, M. Chen, H. Folger, B. Franczak, H. Keller, O. Klepper, B. Langenbeck, F. Nickel, E. Pfeng, M. Pfützner, E. Roeckl, K. Rykaczewski, I. Schall, D. Schardt, C. Scheidenberger, K.-H. Schmidt, A. Schröter, T. Schwab, K. Sümmerer, M. Weber, G. Münzenberg, T. Brohm, H.-G. Clerc, M. Fauerbach, J.-J. Gaimard, A. Grewe, E. Hanelt, B. Knödler, M. Steiner, B. Voss, J. Weckenmann, C. Ziegler, A. Magel, H. Wollnik, J. P. Dufour, Y. Fujita, D. J. Vieira, and B. Sherril, Nucl. Instrum. Methods Phys. Res. B **70**, 286 (1992).

[14] E. Hanelt, T. Brohm, H.-G. Clerc, B. Knoedler, K.-H. Schmidt, M. Steiner, and B. Voss, GSI scientific report 1989 (1990), p. 279; C. Ziegler, T. Brohm, H.-G. Clerc, H. Geissel, K.-H. Schmidt, K. Sümmerer, D. J. Vieira, and B. Voss, GSI scientific report 1990 (1991), p. 291.

[15] S. Kox, A. Gamp, C. Perrin, J. Arvieux, R. Bertholet, J. F. Bruandet, M. Buenerd, Y. El Masri, N. Longequeue, and F. Merchez, Phys. Lett. **159B**, 15 (1985).

[16] K. Zeitelhack, J. Friese, H.-J. Körner, J. Reinhold, and R. Schneider, Nucl. Instrum. Methods Phys. Res. A **333**, 458 (1993).

[17] Th. Stöhlker, H. Geissel, H. Folger, C. Kozhunharov, P. H. Mokler, G. Münzenberg, D. Schardt, Th. Schwab, M. Steiner, H. Stelzer, and K. Sümmerer, Nucl. Instrum. Methods Phys. Res. B **61**, 408 (1991).

[18] Th. Schwab, H. Geissel, M. Chen, H. Folger, A. Magel, F. Nickel, M. Steiner, K. Sümmerer, and G. Münzenberg, GSI scientific report 1990 (1991), p. 290.

[19] Th. Schwab, Ph.D thesis, University Gießen Report No. GSI-91-10, 1991 (unpublished).

[20] K. Sümmerer, J. Reinhold, M. Fauerbach, J. Friese, H. Geissel, H.-J. Körner, G. Münzenberg, R. Schneider, and K. Zeitel-hack, Phys. Rev. C **52**, 1106 (1995).

[21] K.-H. Schmidt, K. Sümmerer, H. Geissel, G. Münzenberg, F. Nickel, M. Pfützner, M. Weber, B. voss, T. Brohm, H.-G. Clerc, M. Fauerbach, J.-J. Gaimard, A. Grewe, E. Hanelt, M. Steiner, J. Weckenmann, C. Ziegler, and A. Magel, Nucl. Phys. **A542**, 699 (1992).

[22] B. Blank, S. Andriamonje, R. Del Moral, J. P. Dufour, A. Fleury, T. Josso, M. S. Pravikov, S. Czajkovski, Z. Janas, A. Piechaczek, E. Roeckl, K.-H. Schmidt, K. Sümmerer, W. Trinder, M. Weber, T. Brohm, A. Grewe, E. Hanelt, A. Heinz, A. Junghans, C. Rdohl, S. Steinhäuser, B. Voss, and M. Pfützner, Phys. Rev. C **50**, 2398 (1994).

[23] R. Schneider, J. Friese, J. Reinhold, K. Zeitelhack, T. Faester-mann, R. Gernhäuser, H. Gilg, F. Heine, J. Homolka, P. Kienle, H. J. Körner, H. Geissel, G. Münzenberg, and K. Süm-merer, Z. Phys. A **348**, 241 (1994).

[24] R. Schneider, T. Faestermann, J. Friese, R. Gernhäuser, H. Gilg, F. Heine, J. Homolka, P. Kienle, H. J. Körner, J. Rein-hold, K. Zeitelhack, H. Geissel, G. Münzenberg, and K. Süm-merer, Phys. Scr. **T56**, 67 (1995).

[25] R. Schneider, T. Faestermann, J. Friese, R. Gernhäuser, H. Geissel, H. Gilg, F. Heine, J. Homolka, P. Kienle, H. J. Kör-ner, G. Münzenberg, J. Reinhold, K. Sümmerer, and K. Zeitel-hack, Nucl. Phys. **A588**, 191c (1995).

[26] W. B. Christie, J. L. Romero, F. P. Brady, C. E. Tull, G. P. Grim, B. McEachern, J. C. Young, H. J. Crawford, D. E. Greiner, P. J. Lindstrom, H. Sann, and U. Lynen, Phys. Rev. C **48**, 2973 (1993).

[27] D. E. Greiner, P. J. Lindstrom, H. H. Heckmann, Bruce Cook, and F. S. Bieser, Phys. Rev. Lett. **35**, 152 (1975).

[28] A. S. Goldhaber, Phys. Lett. **53B**, 306 (1974).

[29] E. J. Moniz, I. Sick, R. R. Whitney, J. R. Ficenec, R. D. Kephart, and W. P. Tower, Phys. Rev. Lett. **26**, 445 (1971).

[30] E. Hanelt, A. Grewe, K.-H. Schmidt, T. Brohm, H.-G. Clerc, M. Dornik, M. Fauerbach, H. Geissel, A. Magel, G. Münzen-berg, F. Nickel, M. Pfützner, C. Scheidenberger, M. Steiner, K. Sümmerer, B. Voss, M. Weber, J. Weckenmann, and C. Ziegler, Z. Phys. A **346**, 43 (1993).

[31] D. J. Morrissey, Phys. Rev. C **39**, 460 (1989).

[32] C. Donzaud, L. Tassan-Got, C. Stephan, D. Bachelier, C. O. Bacri, R. Bimbot, B. Borderie, J. L. Boyard, F. Clapier, T. Hennino, M. F. Rivet, P. Roussel, D. Bazin, C. Grunberg, D. Disdier, B. Lott, and C. Volant, Nucl. Phys. **A593**, 503 (1995).